Gold Nanocone Near-Field Scanning Optical Microscopy Probes

Monika Fleischer,[†,*] Alexander Weber-Bargioni,[‡] M. Virginia P. Altoe,[‡] Adam M. Schwartzberg,[‡] P. James Schuck,[‡] Stefano Cabrini,[‡] and Dieter P. Kern[†]

[†]Institute for Applied Physics, University of Tübingen, Auf der Morgenstelle 10, 72076 Tübingen, Germany and [‡]Molecular Foundry, Lawrence Berkeley National Laboratory, 1 Cyclotron Road, Berkeley, California 94720, United States

ABSTRACT Near-field scanning optical microscopy enables the simultaneous topographical and subdiffraction limited optical imaging of surfaces. A process is presented for the implementation of single individually engineered gold cones at the tips of atomic force microscopy cantilevers. These cantilevers act as novel high-performance optical near-field probes. In the fabrication, thin-film metallization, electron beam induced deposition of etch masks, and Ar ion milling are combined. The cone constitutes a well-defined highly efficient optical antenna with a tip radius on the order of 10 nm and an adjustable plasmon resonance frequency. The sharp tip enables high resolution topographical imaging. By controllably varying the cone size, the resonance frequency can be adapted to the application of choice. Structural properties of these sharp-tipped probes are presented together with topographical images recorded with a cone probe. The antenna functionality is demonstrated by gathering the near-field enhanced Raman signature of individual carbon nanotubes with a gold cone scanning probe.

KEYWORDS: near-field scanning optical microscopy · nanostructures · gold nanocones · electron beam induced deposition · ion milling · near-field enhancement · tip-enhanced Raman spectroscopy

Metallic nanoparticles are of great interest for their ability to sustain localized surface plasmon resonances when interacting with a resonant electromagnetic field.[1−4] The particles can act as antennas for the incoming light, where the external field induces collective oscillations of the conducting electrons.[5−7] These plasmons are accompanied by an evanescent near-field exponentially decaying within tens of nanometers of the metal surface. When the resonance frequency of the optical antenna corresponds to the frequency of excitation, the near-field can be enhanced by several orders of magnitude. The optical near-field is effectively localized to the dimension of the small particle, thus beating the diffraction limit. In this way, light can be directed and controlled at the nanometer scale.

Gold particles with diameters below 100 nm exhibit plasmon resonance frequencies in the visible light spectrum. Making use of such plasmonic particles paves the way to exciting applications in opto-electronic circuits, light harvesting for solar cells, nanolithography, data storage, high sensitivity biosensing, and not least of all, high resolution near-field scanning optical microscopy (NSOM).[8−10] NSOM enables simultaneous high-resolution topographical and subdiffraction limited optical mapping of surfaces. The present work focuses on the fabrication of NSOM scanning probes. To demonstrate their functionality, the near-field enhancement is harnessed for tip-enhanced Raman spectroscopy (TERS).[11−13] TERS can be applied for chemical mapping down to the single molecule level.[14] Both the resolution and the near-field enhancement depend strongly on the properties of the scanning probe. The lateral topographical and optical resolutions directly correlate with the probe tip radius. The plasmon resonance frequency of the NSOM probe depends on the tip geometry, material, dimensions, and radius of curvature, as well as the dielectric properties of the immediate surroundings, including the sample material.[15] Therefore, the quality of the experimental results depends critically on well-suited probe tips.

Recently, significant effort has gone into the design and specific engineering of optimized scanning probes. Most commonly, apertureless scanning probes consist in electrochemically etched gold wires[16] or scanning probes covered with a thin metal layer. To create a more well-defined, strongly localized light-source at the probe tip, single gold or silver spheres or rods have been placed on cantilevers and glass fiber tips, or metallic films have been etched into shape by focused ion beam milling.[17−27] Alternatively, bowtie antennas have been added at the apex of cantilever tips.[28,29] However, the ultimate goal of reproducibly fabricating specifically engineered, high purity optical antennas with ultrahigh topographic resolution on scanning probes has not been achieved yet.

* Address correspondence to monika.fleischer@uni-tuebingen.de.

Received for review August 29, 2010 and accepted February 24, 2011.

Published online March 14, 2011
10.1021/nn102199u

Conical gold shapes are excellent candidates for this purpose, since they combine a sharp tip conducive to highly localized near-fields and high lateral resolution with a larger body of variable size by which the resonance of the antenna can be adjusted. It was shown that gold cones with a height and base diameter on the order of 100 nm can be efficiently excited by a He−Ne-laser beam (wavelength λ = 632.8 nm) polarized parallel to the cone axis.[30−32] In confocal imaging, single cones were observed to effect an enhancement of the gold photoluminescence intensity on the order of a factor of 10 over the full focus area. This corresponds to an intensity enhancement factor on the order of 10^3 when normalized to the area of the near-field spot.[30,33] By dark field spectroscopy it was shown that the resonance wavelength of cones with a height from 10 to 170 nm varies systematically between about 500 and 700 nm and can therefore be adapted to a large part of the visible spectrum. However, most processes presented for the fabrication of gold cones at well-defined positions so far are restricted to planar surfaces.[33−37]

RESULTS AND DISCUSSION

In the present approach, a single gold cone with a base diameter and height on the order of 100 nm is chosen as the antenna and positioned at the apex of a Si_3N_4 cantilever tip. When optically excited, the cone acts as an optical antenna with a strong near-field enhancement near the cone apex. The cone geometry combines a sharp tip radius down to less than 10 nm for high spatial resolution with a larger body for efficient antenna excitation. By tuning the size of the cone, the plasmon resonance frequency can be tailored according to application. To fabricate the gold cone probes, a previously developed method for the fabrication of planar arrays of cones was combined with a process for positioning bowtie antennas on cantilever tips.[29,34] This leads to a precise placement of high purity gold cones. The composition and microscopic structure of the gold cone tips was investigated by transmission electron microscopy, and their topographical and optical performance was evaluated.

Fabrication of Nanocone Probes. The fabrication of the gold cone probes is based on a combination of two newly developed processes, one for the fabrication of gold cones on a flat surface, and the second for the fabrication of bow-tie antennas on cantilever tips (induced deposition mask lithography, IDML).[29,33,34] The process for cone fabrication, which is based on electron beam lithographical patterning of local etch masks, leads to well-defined cones with sub-10 nm tip radii. The related IDML enables the precise positioning of predefined etch masks on arbitrarily shaped surfaces. Schematics of the IDML process and resulting cones for the example of a flat substrate are shown in Figures 1 and 2. By combining the two processes it is possible to place one sharp-tipped gold cone antenna at the apex of a commercial cantilever tip, thus creating a well-defined novel near-field scanning probe.

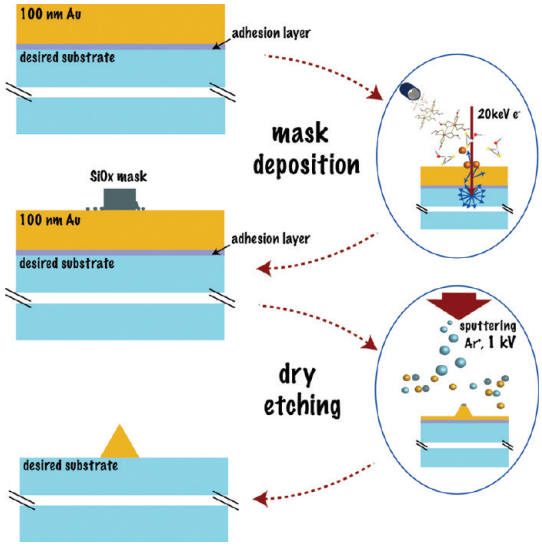

Figure 1. Schematic process for the fabrication of gold nanocones by metallization, focused electron beam induced deposition of an etch mask, and Ar ion milling.

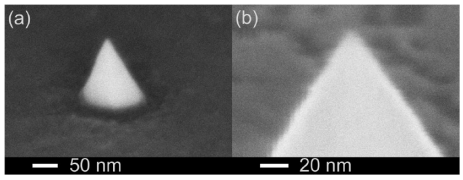

Figure 2. (a) Sharp-tipped gold cone on flat silicon substrate fabricated by IDML and ion milling, (b) gold cone apex with sub-10 nm tip radius. Viewing angle 54° with respect to the perpendicular.

For the combined process, the tip of the pyramidal probe of an atomic force microscopy (AFM) cantilever is widened into a plateau by focused ion beam milling to accommodate a gold cone of ~100 nm base diameter. The trimmed cantilever is covered with a Cr adhesion layer and Au layer (Figure 3a). By using focused electron beam induced deposition (FEBID), a silicon oxide pillar is grown on the metalized plateau (Figure 3a).[38] The pillar serves as an etch mask for the underlying gold layer. An Ar ion beam is applied at perpendicular incidence to remove the etch mask as well as the surrounding metal. During sputtering, the etch mask and gold below the mask together take on a conical shape with the side-wall angle corresponding to the angle of highest sputtering yield.[33,39,40] Removal of the mask by continued etching results in a gold cone of about 10 nm tip radius (Figures 3b,c and 4). In an alternative, additive instead of subtractive, approach a gold pillar can be deposited directly on the cantilever tip by FEBID using a gold precursor.[41,42] However, such deposited gold is strongly contaminated by carbon

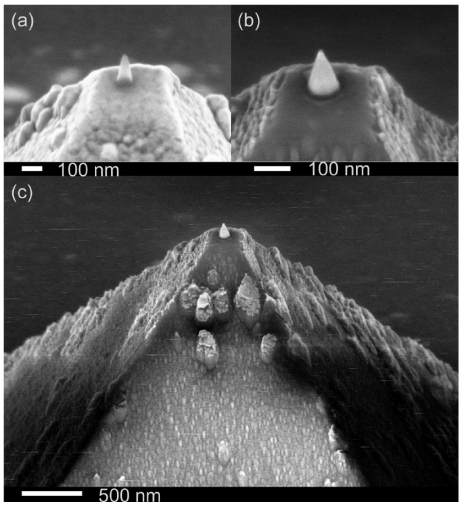

Figure 3. (a) FEBID-fabricated pillar-shaped SiO_x etch mask on the gold-covered plateau of a cantilever tip, (b) gold cone on the plateau of a cantilever tip after etching, with a residual conducting Cr layer covering the tip, (c) overview over the gold cone scanning probe. Viewing angle 54° with respect to the perpendicular. The rough surface of the cantilever pyramid side-walls is inherent to the as-bought Si_3N_4-cantilevers and not related to the cone fabrication process.

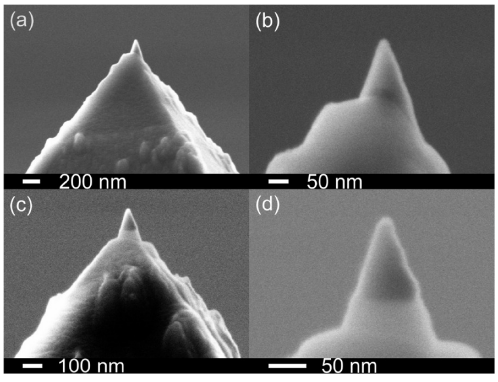

Figure 4. Two examples of final gold cone probes, with overviews over the probe structures (a,c) and high magnification secondary electron images of the gold cone tips (b, d); viewing angle 90°. By the end of the Ar ion etching step, the surrounding Cr and Au layers on the plateau are fully removed. The cones are electrically isolated from the residual metal layer on the side-walls of the cantilever pyramid.

incorporation, which is detrimental for its plasmonic properties. Additionally, sharp tips are hard to achieve by direct deposition.

Since tip radii down to less than 5 nm were achieved using the same subtractive technique on planar substrates, it is to be expected that the cone tip radii can still be reduced. The gold cone tip reestablishes the original minute tip radius of the AFM probe for high-resolution topography imaging. At the same time, it constitutes a well-defined near-field scanning optical microscopy probe with an adjustable plasmon resonance frequency and an area of strong near-field enhancement near the tip apex.[30]

In this work the feasibility of the gold cone probes is demonstrated for the first time. Thirty-one cone tips were fabricated on four sets of cantilevers, which were partly processed in separate work flows. The biggest challenge proved to be the alignment of the etch mask on the plateau. This resulted in four probes without any visible etch mask and four probes with masks placed next to the edge outside the plateau. This technicality however should be easily overcome in a routine process. All the remaining probes displayed sharp-tipped gold cones with tip radii of about 10 nm and a height of about the original deposited gold thickness. Such control over the sharpness of the tips is not easily reached in electrochemically etched probes, and no control of the shape of the plasmonic islands is possible in thermally treated metallic thin-film probes. Moreover, this process opens up the possibility of batch processing on the wafer level, where a large number of cantilevers with truncated pyramid tips could be metalized in one step and treated in a routine, albeit serial, process afterward to obtain well-defined gold cone probes.

Characterization by Transmission Electron Microscopy. The structural properties of several gold cone tips were investigated by transmission electron microscopy (TEM). From the TEM images, the tip radius of the cones can be determined to be about 10 nm (see Figure 5). The cones are proven to consist of pure gold, and exhibit fringes characteristic of Au crystal planes. The cone surfaces are covered by an approximately 2 nm thick layer of amorphous lower atomic mass material that is stable under observation with the electron beam. This is thought to be a redeposition layer typical for dry etching processes, which contains a mixture of all materials present during the sputtering process.[43] In one case (Figure 5, right), some residual SiO_x etch mask was observed on the cone tip, which was gradually removed by the high energy electron beam during imaging.

The diffraction patterns (Figure 6a,b) of two cones show diffraction rings characteristic of polycrystalline gold, with one dominant crystal orientation each. In the first case the dominant orientation is Au (022), in the second, Au (002) is dominant. The observed interplanar spacings, d, agree with the bulk literature values $d = 1.442$ Å for Au (022) and $d = 2.039$ Å for Au (002) to within 2%.[44] For dark field TEM imaging, only the reflections associated with Au (022) and Au (002) are selected. The corresponding domains of the cones appear bright in the dark field images, Figure 6c,d. In both cases, the cones are polycrystalline, while a large part of the cone consists of one single crystalline grain. The dark areas of the cones in the dark field images correspond to grains in different orientations.

Using energy dispersive X-ray spectroscopy (X-ray EDS) for elemental analysis, the element distribution within the pyramid and gold cone region was

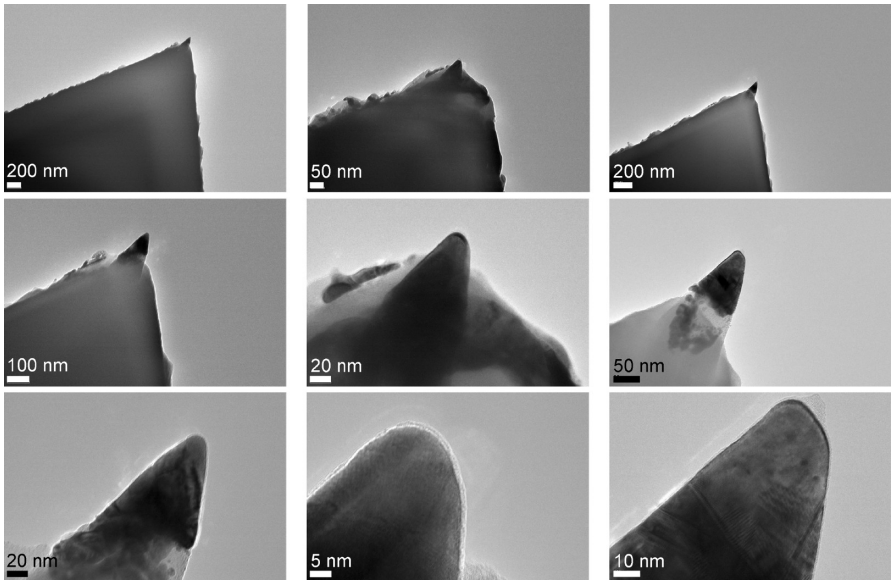

Figure 5. Bright field TEM images of three different gold cone tips (left, middle, and right column) at increasing magnification from top to bottom row. Dark cone areas correspond to gold. Left: Well-centered gold cone, about 20 nm tip diameter. Center: Slightly off-centered gold cone, about 20 nm tip diameter. The gold cone is covered by a bright amorphous 2 nm layer of a different material, presumably as a result of redeposition from the ion milling process. Right: Well-centered well-defined gold cone, slightly under-etched. Few nanometers of residual bright SiO_x etch mask can still be discerned on the cone tip, which is not yet done sharpening. Moiré fringes mark crystallinity. The straight line toward the bottom of the cone corresponds to an interface between Au grains with different crystal orientations.

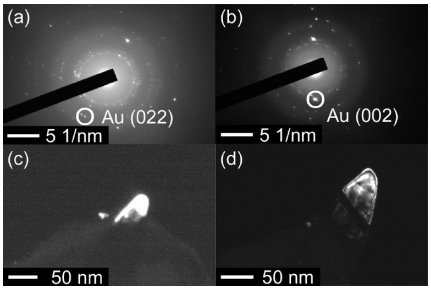

Figure 6. Diffraction patterns and dark field TEM images of two cone tips. Dominant reflections occur that correspond to crystal orientations (a) Au (022) with an interplanar spacing of $d_{(022)}$ = 1.442 Å, and (b) Au (002) with $d_{(002)}$ = 2.039 Å. The respective reflections are selected to create the dark field images (c,d), in which only areas with the chosen orientations appear bright. Both tips largely consist of one single crystalline domain, with different domains further down the cone. Again, the interface between Au grains with different crystal orientations is evident in panel d.

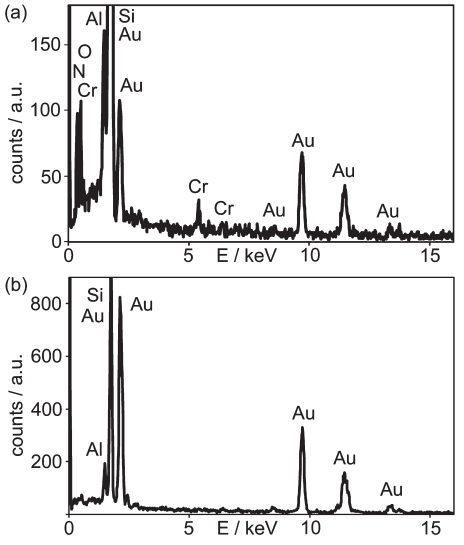

Figure 7. X-ray EDS spectra recorded (a) from the cantilever tip area including the front end of the Si_3N_4 cantilever and the full gold cone area for 48.4 s, and (b) selective spectrum from the gold cone tip only (40.1 s). In panel a all elements present can be seen (Si, N, Cr, O, Au, Al), while in the cone region, except for some Si and Al scattering from the bulk of the cantilever and cantilever holder, respectively, purely Au is registered. In spite of previous intense imaging of the gold cone tips in an SEM, no carbon contamination is detected.

investigated (see spectra in Figure 7 and element distribution maps in Figure 8). The images show the expected Si and N distribution within the cantilever pyramid area (Figure 8 panels a2, a3, b2, b3), some Cr and Au residues on the pyramid side-wall (Figure 8a4), the Cr adhesion layer at the bottom of the cone (Figure 8b5), and traces of implanted Ga only in the side-wall that was imaged for focused ion beam alignment (Figure 8a5). The cone is exclusively composed of gold (Figures 8 panels a4, b4) as confirmed by spectra taken at the position of the cone tip (Figure 7b).

Characterization by TEM imaging provides valuable insights into the effects of different processing steps on the structural properties, as well as into the morphology of the final gold cone probes.

Measurements Using Cone Probes. The topographical resolution that can be obtained with the gold cone scanning probes was investigated by employing them as regular contact mode AFM probes. They were

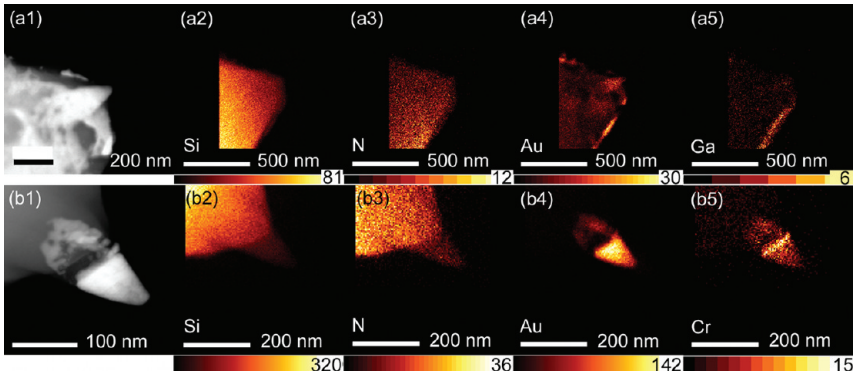

Figure 8. Element-specific maps of two cone tip regions obtained from the X-ray EDS spectra. (a1,b1) High-angle annular dark field (HAADF-STEM) images of the cone tips; bright areas correspond to gold cones. (a2,b2) Si signal is restricted to the cantilever region, except for slight artifacts in (b2) due to bulk material scattering. (a3,b3) N is restricted to the cantilever region. (a4) Au is present in the gold cone, with some residual gold on the cantilever pyramid walls, (b4) Au is clearly present in the gold cone only. (a5) Some Ga contamination from the FIB milling is visible on the wall of the cantilever imaged for the plateau cutting, but none in the region of the cone, which was fabricated subsequently. (b5) The Cr adhesion layer is distinctly visible below the gold.

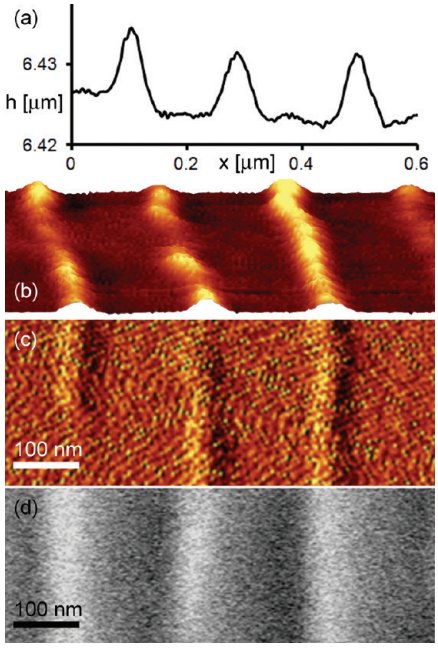

Figure 9. Images of lithographically patterned PMMA lines, width, ∼45 nm; pitch, ∼200 nm; height, ∼10 nm. (a−c) Gold cone tip contact mode AFM images: (a) linescan, (b) 3D topography, (c) feedback image, (d) SEM image.

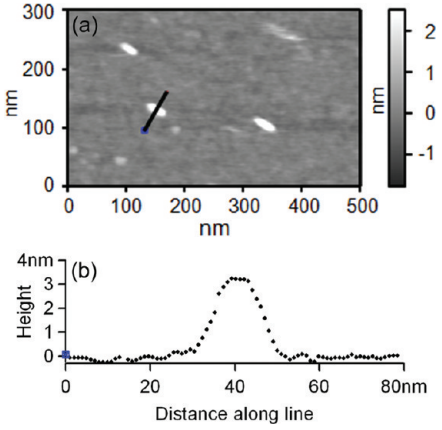

Figure 10. (a) Gold cone tip contact mode AFM image of individual 4 nm high and wide, about 20 nm long, CdS nanorods dispersed on a Si substrate; (b) linescan along the line indicated in panel a.

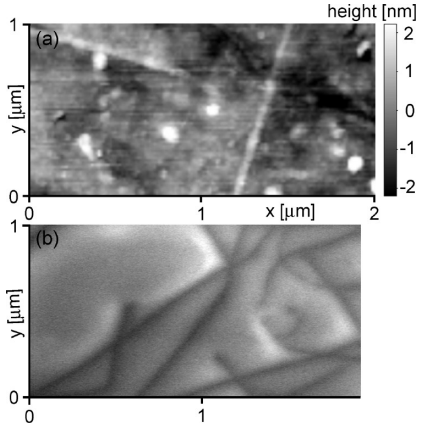

Figure 11. (a) Gold cone tip contact mode AFM image and (b) SEM image of dilute carbon nanotubes on two fused silica samples. In the SEM image, the nanotubes appear dark and larger than their actual size due to potential contrast.

mounted for scanning different samples, like regularly patterned polymethyl-methacrylate (PMMA) resist lines, CdS nanorods dispersed on a Si substrate, and dilute carbon nanotubes on cover glass substrates. As can be seen in Figures 9 −11, topography scans with a resolution on the order of 10 nm were achieved with the gold cone probe tips. In Figure 9, the PMMA lines are shown in the scanning electron microscope (SEM) image to have a pitch of about 200 nm and line widths of about 45 nm. In the gold cone probe topography image, they are well resolved with a varying apparent line width of 40−60 nm and a height of about 10 nm. In the scan of the short CdS nanorods in Figure 10, the height and flat top of nominally 4 nm each are clearly reflected. The apparent width at the bottom of the

structures is 15−20 nm as measured from line cuts as shown in Figure 10b. From the known shape in conjunction with the apparent width and slope of the side walls, the tip radius of the cone tips can be deduced to be about 10 nm, which is consistent with the radius observed in TEM. On the dilute carbon nanotube sample (Figure 11), few nanotubes are present per square micrometer. Two nanotubes can be discerned in the gold cone probe topography scan, Figure 11a. Because of charging effects, the carbon nanotubes appear wider than their actual size in the SEM image (Figure 11b), and display strong potential contrast.[45,46] The above examples therefore show that the gold cone probes are well suited for high-resolution topography imaging with a resolution on the order of the cone tip radius.

To evaluate the stability and tuneability of the plasmonic properties of the gold cones, dark field scattering spectroscopy of individual nanocones was performed. Since the setup works in transmission, and reasonable statistics and a well-defined focal plane were desired, the experiments were performed on a large number of individual gold cones on planar glass substrates rather than on individual gold cone probes on opaque cantilevers. This fact changes the absolute values of the plasmon resonance wavelength due to the different index of refraction of the respective substrates, but not the basic fact of the demonstrated tuneability. The plasmon resonance wavelength and the dark field scattering intensity were evaluated for 12 arrays of 16 cones each, fabricated with the same nominal size of a base diameter of 95 nm and a height of 85 nm. The plasmon resonance wavelength (wavelength of maximum scattering intensity) proved to be highly reproducible at 566 ± 6 nm across all spectra, while the value of the maximum scattering intensity (which also depends on the focus settings) varied by about 10% to 20% within each array. To demonstrate the tuneability of the plasmon resonance wavelength by means of the cone size, cones of different heights were investigated. The results are displayed in Figure 12. As can be seen, the resonance depends roughly linearly on the height and can be adapted over a wide range of the visible spectrum by predetermining the corresponding cone height *via* the initial gold layer thickness. In the present case the (nominally constant)[33] aspect ratio (height divided by base diameter) was observed to decrease with decreasing height due to overetching for small cones. The respective influence of the two parameters still remains to be separated. The potential of being adapted to different wavelengths while maintaining their small tip radius sets the cone tip probes apart from their chemically etched or thermally treated thin-film counterparts.

The most important purpose of the gold cone probes is to obtain high-resolution high intensity near-field optical images. To evaluate the near-field

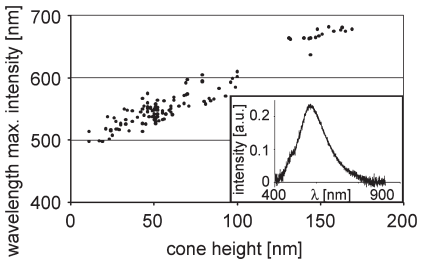

Figure 12. Dependence of the plasmon resonance wavelength on the cone height. Dark field scattering spectra are taken for individual gold cones on planar glass substrates, and the wavelength of maximum scattering intensity is plotted *versus* the cone height. The resonance can be tuned over 200 nm of the visible spectrum with an approximately linear dependence on the cone height. Inset: sample dark field spectrum of a single 90 nm high gold cone with 95 nm base diameter, 30 s integration time.

enhancement properties, the carbon nanotube sample was scanned under the cone tip, while a near-field enhanced Raman spectrum was collected at each position. Characteristic peaks in the Raman spectra act as a fingerprint of the carbon nanotubes. In particular, the D-band around 1340−1370 cm^{-1} results from disordered carbon, while the G-band around 1560−1600 cm^{-1} is close to the value of the doubly degenerate Raman-active vibrational mode for graphite at 1582 cm^{-1}.[47] The three-dimensional spectral map of the sample can be spectrally filtered by means of the imaging software. This way, the spatial distribution of the signal collected from the G-band region from 1555 to 1600 cm^{-1} was extracted. Local variations of the G-band signal were apparent in the image, with regions of increased G-band intensity. However no spatial resolution of the carbon nanotubes could be obtained. Because of strong interaction between the nanotubes and scanning probe, nanotubes were dragged along by the tip, as becomes apparent in the topography scans. The measurements were restricted to contact mode scans, since contact mode AFM cantilevers were chosen for the cone tips because of their less extreme topography and the expected highest Raman signal in contact. For future experiments, the scan parameters and sample preparation can be optimized, or noncontact cantilevers can be prepared and measured in a lock-in setup.

Looking at the individual spectra instead, one sees a broadly distributed nonspecific emission background resulting from the gold tip, and a higher harmonic of the laser line at around 175 cm^{-1} (Figure 13a).[48] In experiments using sharp-tipped cones on planar substrates for Raman spectroscopy, strong gold luminescence background is regularly observed owing to the high electric field strength at the cone apex. In the case of the cone tip probes, the background is increased by residual gold on the sides of the cantilever pyramid due to a high sidewall roughness of the as-bought cantilevers, which could not easily be removed (see

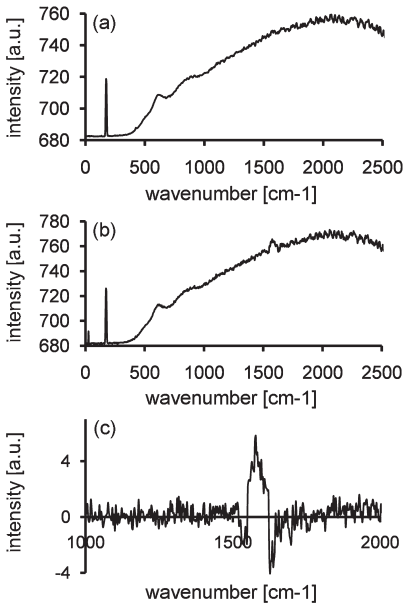

Figure 13. Photoluminescence background and Raman intensity measured with a gold cone probe on a dilute carbon nanotube sample. A higher harmonic of the blocked laser mode is present at 175 cm^{-1}. At most sample positions, no Raman lines are visible above the photoluminescence background (a). In particular sample positions a line reproducibly shows up at 1550 to 1600 cm^{-1}, corresponding to the G-band signature of ordered carbon (b). The data shown are averaged over several similar characteristic spectra at different sample positions each. In panel c the difference between the two normalized averaged spectra is displayed, exhibiting just the G-band signature.

Figure 3). Some residual gold is present in the confocal laser focus, adding to the background. The background luminescence only exhibits the shown stable spectral distribution when the tip is in the focus, hence confirming the tip as the major source of luminescence.

For the spectra with increased G-band signal, a distinct additional peak is present at around 1550–1605 cm^{-1}, as shown in Figure 13b. The peak is reproducibly observed for particular sample positions, and is attributed to the presence of individual carbon nanotubes. For most sample positions it disappears, as can be seen in Figure 13a. The area of excitation with the low laser power of 30 μW is only the very small area of less than $A_{NF} \approx \pi \times (10\ nm)^2$ directly below the gold cone probe, as confirmed by numerical simulations for extended probes as well as for the present cone geometry.[49,50]

In contrast, the confocal spot diameter when the near-field probe is removed is diffraction-limited to about $d_C \approx 0.51 \times \lambda/NA = 0.51 \times 632.8\ nm/1.4 \approx 230\ nm$. The illuminated area in the confocal case is therefore at least $A_C \approx \pi \times (115\ nm)^2$. For both confocal and near-field excitation, the G-band Raman intensity originates only from the Raman active fractions of the illuminated areas that are covered with nanotubes. Assuming one single diametrically positioned nanotube with an average width of $w \approx 1.6$ nm, this leads to active areas of $A^*_{NF} \approx 20\ nm \times w$ for the near-field case, and $A^*_C \approx 230\ nm \times w$ for the confocal case. The near-field enhancement factor for the Raman intensity, R_{NF}, is defined as the ratio of collected G-band Raman signals I_{NF} and I_C for the near-field and the confocal case at identical laser power and integration time, and normalized by the respective excitation areas. It can be roughly estimated as

$$R_{NF} = \frac{I_{NF}}{A^*_{NF}} / \frac{I_C}{A^*_C} = (I_{NF}/I_C)(A^*_C/A^*_{NF}) \approx (I_{NF}/I_C) \times 230/20$$
$$\approx (I_{NF}/I_C)12$$

To see a distinct signature of comparable intensity in confocal spectra as in the near-field spectra however, the same sample needs to be excited with a laser power on the order of mW. Assuming a linear dependence of the measured intensities on the excitation power,[51,52] the ratio I_{NF}/I_C at identical power is equivalent to the increase in power P_C/P_{NF} necessary to observe comparable signal strengths $I_{NF} \approx I_C$. This leads to an estimated

$$R_{NF} \approx (P_C/P_{NF})(A^*_C/A^*_{NF}) \approx 100 \times 12 \approx 1200$$

for the realistic example of $P_C \geq 3$ mW. This evaluation is fraught with uncertainty, since the real distribution of the dispersed carbon nanotubes in the illuminated areas and the mean value of P_C are unknown, but it can be considered a lower limit. In the experimental setup, the confocal spot is usually bigger than the diffraction limit, which makes A^*_C a lower bound for the estimate. If several nanotubes with a total length L_{tot} of more than d_C are present in the confocal spot, the enhancement factor is additionally increased by a factor of L_{tot}/d_C due to the increase of A^*_C. In a recent publication, a power law dependence $I = I_0{*}P^{\alpha}$ of the intensity on the laser power has been reported with a superlinear exponent $\alpha > 1$ for excitation with red light, which would further increase the enhancement factor.[53] It should also be noted that for efficient excitation of the cone, the laser beam was radially polarized such that the electric field components in the focus are predominantly oriented vertically to the substrate.[30] This polarization is not ideal for exciting the carbon nanotubes aligned parallel to the substrate. All in all, the rough estimate shows that the reproducibly observed carbon signature of single nanotubes in tip-enhanced spectra at 30 μW is a clear indication of near-field enhancement by the gold cone tip.

Since the Raman intensity scales approximately with the electric field enhancement as $\mathbf{E}^4$, R_{NF} corresponds to an electric field enhancement factor on the order of 10. This value is of the same order as enhancement factors reported for sharp gold tips fabricated by pulling and electrochemical etching of gold wires.[14,54] The pulled wires however present a less well-defined

geometry with a lower yield of very sharp tips. From previously observed electric field enhancement factors at the cone apex,[30] still higher Raman enhancement factors are expected.

The demonstrated high topographical resolution, near-field enhancement of the Raman intensity in first experiments of $>10^3$ and adjustable resonance frequency of the gold cone probes make them highly interesting as next-generation high-performance near-field scanning optical microscopy probes.

CONCLUSIONS

We demonstrate a process for the reproducible fabrication of well-defined high purity near-field scanning optical microscopy probes. The probes consist of a gold nanocone positioned at the tip of an AFM cantilever pyramid. The gold cones have been shown to act as optical antennas with strong near-field enhancement near the cone apex under laser excitation. Their plasmon resonance frequency is determined by the size of the cone. This near-field probe concept combines the advantages of a very sharp tip for high spatial resolution, and a well-defined and adjustable resonance frequency. The morphology of the gold cone tips was investigated by TEM. High resolution topography scans as well as first near-field enhanced spectra from individual carbon nanotubes were shown to prove the suitability of the gold cone probes as high-performance near-field probes.

METHODS

Commercially available silicon nitride contact-mode AFM cantilevers (NanoWorld) with a cantilever stiffness of 0.2 N/m are used as the starting material. At the front end of the triangular cantilevers, a hollow Si_3N_4 pyramid (base length, 4.0 μm; height, 3.5 μm) of nominally less than 10 nm tip radius serves as the topography probe. The pyramid tip is widened into a plateau of about 200 nm $\times$ 200 nm by focused ion beam milling to accommodate a gold cone of about 100 nm base diameter. Cutting is performed using the focused Ga ion beam of a Zeiss 1540 XB cross beam at 30 keV and 10 pA ion current. Here the inclination angle of the mounted cantilever with respect to the sample surface is taken into account, such that after mounting the cantilever, the plateau will be parallel to the surface. The trimmed cantilever is placed in an evaporator, where a 5 nm Cr adhesion layer and a 100 nm Au layer are thermally evaporated onto the sample. The gold-covered plateau is still well visible at the pyramid tip (Figure 3a). On the gold layer, IDML is performed with a potential feature resolution of less than 10 nm. Using the gas injection system on the cross beam machine, a nozzle supplying the precursor gas pentamethylcyclopentasiloxane ($C_5H_{20}O_5Si_5$) is approached to the cantilever. A 20 keV electron beam is positioned at the center of the plateau and blanked. By means of a pattern generator (Xenos), focused electron beam induced deposition of a silicon oxide pillar is performed.[38] The precursor is decomposed by the backscattered secondary electrons into SiO_x and a volatile component, which is removed by pumping. By referring to a previous dose optimization series,[55] the exposure dose is chosen such that the resulting SiO_x pillar has a base diameter of about 50 nm and a height of 100−300 nm (Figure 3a). This pillar now serves as an etch mask for the underlying gold layer. An NTI argon ion gun was added to the cross beam system to enable *in situ* Ar ion milling. The cantilever and etch mask are bombarded with an Ar ion beam at perpendicular incidence with respect to the plateau for about 20−40 min, depending on the mask height. An etch spot of about 1 mm^2 size is obtained with a 1 keV Ar ion beam at 10 mA beam current. In the process, the Au and Cr on the plateau are removed as well as the etch mask, taking advantage of the higher etch rate of the gold with respect to the mask. Underneath the etch mask, a truncated gold cone with the height of the gold thickness and a base angle of about 60° to 70° is formed due to lateral shrinking of the mask and an angle-dependent sputtering yield of the ion bombardment process.[39,40] The etching progress can be monitored repeatedly by *in situ* SEM imaging. It is continued until the etch mask is just fully removed, which results in a gold cone of about 10 nm tip radius (Figures 3b,c). The mask height needs to be chosen such that ultimately the Au and Cr layer surrounding the cone are fully removed as well, and the cone is electrically isolated from potential residual metal layers on the sides of the Si_3N_4 pyramid (Figure 4). Since the Ar etch rate is reduced on these inclined side-walls, Au and Cr residues may remain on the slopes after etching. Overetching of the plateau is uncritical, but raises the gold cone on a Si_3N_4 platform above the receding plateau. The described method offers a means of fabricating high-purity metal nanostructures with good reproducibility. The high resolution of electron beam lithography is maintained while fabrication can be extended to nonconducting and nonplanar substrates. Compared to conventional focused ion beam milling, the contamination by Ga ions detrimental to the plasmonic properties is prevented.[56]

TEM characterization was performed using a 200 kV field-emission analytical scanning transmission electron microscope (TEM JEOL 2100-F) equipped with an energy dispersive X-ray spectrometer (INCAEnergyTEM250, Oxford). Elemental maps were acquired using a nominal probe size of 1 nm.

Both contact mode atomic force microscopy of PMMA lines (Figure 9) and Raman measurements on carbon nanotubes (Figure 13) were conducted in a Witec alpha 300 confocal Raman/NSOM/AFM microscope. The PMMA lines on cover glass were defined by electron beam lithography in a Vistec VB300-UHR EWF electron-beam lithography system. Dilute carbon nanotube samples were prepared by chemical vapor deposition growth of carbon nanotubes on fused silica cover glass slides. A solution of ferritin with concentrations of ~0.001−0.0001 mg/mL was dripped on the substrate followed by oxidation. The ensuing carbon nanotubes are predominantly single-walled with typical average diameters of about 1.6 nm. Additional contact mode AFM imaging of the carbon nanotubes was provided using an Asylum MFP-3D atomic force microscope (Figure 11). The same instrument was used for gold cone probe contact mode imaging of CdS nanorods on a Si substrate (Figure 10). The chemically synthesized CdS nanorods have a narrow size distribution with widths and heights of about 4 nm. The apparent length of the nanorods measured in Figure 10 is about 36 nm. Taking into account the AFM probe radius, this corresponds to an actual length of about 20 nm. A drop of nanorods dispersed in chloroform solution was applied to a piranha cleaned Si wafer. The sample was rinsed with copious amounts of chloroform and dried in nitrogen flow for SEM and AFM imaging. Multiple contact mode scans of the CdS sample were performed with a single cone probe over the course of several hours during which no considerable deterioration of the image quality was observed.

Dark field spectroscopy was performed with a Nikon Eclipse TE 2000-U inverted microscope with a NA 0.95−0.8 dry dark field condenser and a 60$\times$ NA 0.7 air objective. Arrays of cones were fabricated using the identical process as for the gold cone

tips, but on planar glass substrates. The cones within the 4×4 arrays were spaced at 4−5 μm. By inserting a pinhole at the entrance of the spectrometer (Princeton Instruments Acton Spectra Pro 2300i), a sample area on the order of 1 μm diameter was probed, thus enabling selective spectroscopy of individual cones. The spectra with a typical integration time of 30 s were corrected for the spectrum of the white light lamp as well as background corrected.

For Raman imaging of the carbon nanotubes, a radially polarized He−Ne-laser beam was focused on the gold cone tip through the transparent substrate from below using a 100×, 1.4 NA oil immersion objective. Radial polarization was obtained by means of a liquid crystal *z*-polarizer (radial polarization converter, ARCoptix). In the focus, the laser beam has a strong longitudinal component polarized in the direction of the cone axis. Lateral and vertical alignment of the bottom objective with respect to the tip was effected by maximizing the nonlinear emission background of the gold tip/cone system. The laser power before the objective was reduced to $P_{NF} = 30$ μW, to avoid melting of the gold cone. When scanning the sample, the scattered light was collected by the same objective and passed through a dichroic beam splitter and a 640 nm long pass filter into a spectrometer. While scanning an image area of 3×3 μm^2 (150×150 pixels), a full spectrum over the range 0−2700 cm^{-1} was recorded at each position for 2 s.

Acknowledgment. D. Ghosh, A. Ismach, and S. Dhuey are gratefully acknowledged for providing the CdS nanorod, carbon nanotube, and structured PMMA samples. The authors thank F. Ogletree, P. Ashby, and D. Olynick for valuable discussions. This project is supported by the European Social Fund and by the Ministry Of Science, Research and the Arts Baden-Württemberg. M.F. gratefully acknowledges financial support by the Baden-Württemberg-Stiftung and by Projektförderung für Nachwuchswissenschaftlerlnnen from Tübingen University. Work at the Molecular Foundry was performed under User Proposal No. 550 and supported by the Office of Science, Office of Basic Energy Sciences, of the U.S. Department of Energy under Contract No. DE-AC02-05CH11231.

REFERENCES AND NOTES

1. Novotny, L.; Hecht, B. *Principles of Nano-optics*; Cambridge University Press: New York, 2006.
2. Maier, S. A. *Plasmonics: Fundamentals and Applications*. Springer: Berlin, 2007.
3. Barnes, W. L.; Dereux, A.; Ebbesen, T. W. Surface Plasmon Subwavelength Optics. *Nature* **2003,** *424*, 824–830.
4. Atwater, H. A. The Promise of Plasmonics. *Sci. Am.* **2007,** *296*, 56–62.
5. Mühlschlegel, P.; Eisler, H. J.; Martin, O. J. F.; Hecht, B.; Pohl, D. W. Resonant Optical Antennas. *Science* 2005, *308*, 1607−1609.
6. Schuck, P. J.; Fromm, D. P.; Sundaramurthy, A.; Kino, G. S.; Moerner, W. E. Improving the Mismatch between Light and Nanoscale Objects with Gold Bowtie Nanoantennas. *Phys. Rev. Lett.* **2005,** *94*, 017402.
7. Garcia-Parajo, M. F.; Kino, G.; Zia, R.; Tang, L.; Merlein, J.; Taminiau, T. H.; *et al. Nature Photon.* **2008,** *2* (4), 199–256.
8. Novotny, L.; Stranick, S. J. Near-Field Optical Microscopy and Spectroscopy with Pointed Probes. *Annu. Rev. Phys. Chem.* **2006,** *57*, 303–331.
9. Girard, C. Near Fields in Nanostructures. *Rep. Prog. Phys.* **2005,** *68*, 1883–1933.
10. Bouhelier, A. Field-Enhanced Scanning Near-Field Optical Microscopy. *Microsc. Res. Technol.* **2006,** *69*, 563–579.
11. Stöckle, R. M.; Suh, Y. D.; Deckert, V.; Zenobi, R. Nanoscale Chemical Analysis by Tip-Enhanced Raman Spectroscopy. *Chem. Phys. Lett.* **2000,** *318*, 131–136.
12. Hartschuh, A.; Sanchez, E. J.; Xie, X. S.; Novotny, L. High-Resolution Near-Field Raman Microscopy of Single-Walled Carbon Nanotubes. *Phys. Rev. Lett.* **2003,** *90*, 095503.
13. Pettinger, B.; Ren, B.; Picardi, G.; Schuster, R.; Ertl, G. Nanoscale Probing of Adsorbed Species by Tip-Enhanced Raman Spectroscopy. *Phys. Rev. Lett.* **2004,** *92*, 096101.
14. Domke, K. F.; Zhang, D.; Pettinger, B. Toward Raman Fingerprints of Single Dye Molecules at Atomically Smooth Au(111). *J. Am. Chem. Soc.* **2006,** *128*, 14721–14727.
15. Kuwata, H.; Tamaru, H.; Esumi, K.; Miyano, K. Resonant Light Scattering from Metal Nanoparticles: Practical Analysis beyond Rayleigh Approximation. *Appl. Phys. Lett.* **2003,** *83*, 4625–4627.
16. Eligal, L.; Culfaz, F.; McCaughan, V.; Cade, N. I.; Richards, D. Etching Gold Tips Suitable for Tip-Enhanced Near-Field Optical Microscopy. *Rev. Sci. Instrum.* **2009,** *80*, 033701.
17. Sqalli, O.; Bernal, M.-P.; Hoffmann, P.; Marquis-Weible, F. Improved Tip Performance for Scanning Near-Field Optical Microscopy by the Attachment of a Single Gold Nanoparticle. *Appl. Phys. Lett.* **2000,** *76*, 2134–2136.
18. Kalkbrenner, T.; Ramstein, M.; Mlynek, J.; Sandoghdar, V. A Single Gold Particle as a Probe for Apertureless Scanning Near-Field Optical Microscopy. *J. Microsc.* **2001,** *202*, 72–76.
19. Frey, H. G.; Keilmann, F.; Kriele, A.; Guckenberger, R. Enhancing the Resolution of Scanning Near-Field Optical Microscopy by a Metal Tip Grown on an Aperture Probe. *Appl. Phys. Lett.* **2002,** *81*, 5030–5032.
20. Eah, S.-K.; Jaeger, H. M.; Scherer, N. F.; Wiederrecht, G. P.; Lin, X.-M. Plasmon Scattering from a Single Gold Nanoparticle Collected through an Optical Fiber. *Appl. Phys. Lett.* **2005,** *86*, 031902.
21. Kim, Z. H.; Leone, S. R. High-Resolution Apertureless Near-Field Optical Imaging Using Gold Nanosphere Probes. *J. Phys. Chem. B* **2006,** *110*, 19804.
22. Taminiau, T. H.; Moerland, R. J.; Segerink, F. B.; Kuipers, L.; van Hulst, N. F. Lambda/4 Resonance of an Optical Monopole Antenna Probed by Single Molecule Fluorescence. *Nano Lett.* **2007,** *7*, 28–33.
23. Olk, P.; Renger, J.; Härtling, T.; Wenzel, M. T.; Eng, L. M. Two Particle Enhanced Nano Raman Microscopy and Spectroscopy. *Nano Lett.* **2007,** *7*, 1736–1740.
24. Gan, Y. A Review of Techniques for Attaching Micro- and Nanoparticles to a Probe's Tip for Surface Force and Near-Field Optical Measurements. *Rev. Sci. Instrum.* **2007,** *78*, 081101.
25. Wenzel, M. T.; Härtling, T.; Olk, P.; Kehr, S. C.; Grafström, S.; Winnerl, S.; Helm, M.; Eng, L. M. Gold Nanoparticle Tips for Optical Field Confinement in Infrared Scattering Near-Field Optical Microscopy. *Opt. Express* **2008,** *16*, 12302–12312.
26. De Angelis, F.; Das, G.; Candeloro, P.; Patrini, M.; Galli, M.; Bek, A.; Lazzarino, M.; Maksymov, I.; Liberale, C.; Andreani, L. C.; *et al.* Nanoscale Chemical Mapping Using Three-Dimensional Adiabatic Compression of Surface Plasmon Polaritons. *Nat. Nanotechnol.* **2010,** *5*, 67–72.
27. Zou, Y.; Steinvurzel, P.; Yang, T.; Crozier, K. B. Surface Plasmon Resonances of Optical Antenna Atomic Force Microscope Tips. *Appl. Phys. Lett.* **2009,** *94*, 171107.
28. Farahani, J. N.; Pohl, D. W.; Eisler, H.-J.; Hecht, B. Single Quantum Dot Coupled to a Scanning Optical Antenna: A Tunable Superemitter. *Phys. Rev. Lett.* **2005,** *95*, 017402.
29. Weber-Bargioni, A.; Schwartzberg, A. M.; Schmidt, M.; Harteneck, B; Ogletree, D. F.; Schuck, P. J.; Cabrini, S. Functional Plasmonic Antenna Scanning Probes Fabricated by Induced-Deposition Mask Lithography. *Nanotechnol.* **2010,** *21*, 065306.
30. Fleischer, M.; Stanciu, C.; Stade, F.; Stadler, J.; Braun, K.; Heeren, A.; Häffner, M.; Kern, D. P.; Meixner, A. J. Three-Dimensional Optical Antennas: Nanocones in an Apertureless Scanning Near-Field Microscope. *Appl. Phys. Lett.* **2008,** *93*, 111114.
31. Zhang, D.; Wang, X.; Braun, K.; Egelhaaf, H.-J.; Fleischer, M.; Hennemann, L.; Hintz, H.; Stanciu, C.; Brabec, C. J.; Kern, D. P.; *et al.* Parabolic Mirror-Assisted Tip-Enhanced Spectroscopic Imaging for Nontransparent Materials. *J. Raman. Spectrosc.* **2009,** *40*, 1371–1376.
32. Zeeb, B.; Jäger, S.; Schäfer, C.; Nill, P.; Meixner, A. J.; Kern, D. P.; Fleischer, M. Gold Nanocone Probes for Near-Field Scanning Optical Microscopy. *J. Vac. Sci. Technol., B* **2010,** *28*, C6O34–C6O37.

33. Fleischer, M.; Zhang, D.; Braun, K.; Jäger, S.; Ehlich, R.; Häffner, M.; Stanciu, C.; Hörber, J. K. H.; Meixner, A. J.; Kern, D. P. Tailoring Gold Nanostructures for Near-Field Optical Applications. *Nanotechnology* **2010,** *21*, 065301.
34. Stade, F.; Heeren, A.; Fleischer, M.; Kern, D. P. Fabrication of Metallic Nanostructures for Investigating Plasmon-Induced Field Enhancement. *Microelectron. Eng.* **2007,** *84*, 1589–1592.
35. Fleischer, M.; Stade, F.; Heeren, A.; Häffner, M.; Braun, K.; Stanciu, C.; Ehlich, R.; Hörber, J. K. H.; Meixner, A. J.; Kern, D. P. Nanocones on Transparent Substrates for Investigations in Scanning Probe Microscopes. *Microelectron. Eng.* **2009,** *86*, 1219–1221.
36. Kim, T. I.; Kim, J. H.; Son, S. J.; Seo, S. M. Gold Nanocones Fabricated by Nanotransfer Printing and Their Application for Field Emission. *Nanotechnology* **2008,** *19*, 295302.
37. Kontio, J. M.; Simonen, J.; Tommila, J.; Pessa, M. Arrays of Metallic Nanocones Fabricated by UV-Nanoimprint Lithography. *Microelectron. Eng.* **2010,** *87*, 1711–1715.
38. Utke, I.; Hoffmann, P.; Melngailis, J. Gas-Assisted Focused Electron Beam and Ion Beam Processing and Fabrication. *J. Vac. Sci. Technol., B* **2008,** *26*, 1197–1276.
39. Stewart, A. D. G.; Thompson, M. W. Microtopography of Surfaces Eroded by Ion-Bombardment. *J. Mater. Sci.* **1969,** *4*, 56–60.
40. Vossen, J. L. The Preparation of Substrates for Film Deposition Using Glow Discharge Techniques. *J. Phys. E: Sci. Instrum.* **1979,** *12*, 159–167.
41. Utke, I.; Hoffmann, P. Focused Electron Beam Induced Deposition of Gold. *J. Vac. Sci. Technol. B* **2000,** *18*, 3168–3171.
42. Squalli, O.; Utke, I.; Hoffmann, P.; Marquis-Weible, F. Gold Elliptical Nanoantennas as Probes for Near Field Optical Microscopy. *J. Appl. Phys.* **2002,** *92*, 1078–1083.
43. Glöersen, P. G. Ion-Beam Etching. *J. Vac. Sci. Technol.* **1975,** *12*, 28–35.
44. Edington, J. W. *Practical Electron Microscopy in Materials Science*; Van Nostrand Reinhold Co: New York, 1976.
45. Brintlinger, T.; Chen, Y. F.; Dürkop, T.; Cobas, E.; Fuhrer, M. S.; Barry, J. D.; Melngailis, J. Rapid Imaging of Nanotubes on Insulating Substrates. *Appl. Phys. Lett.* **2002,** *81*, 2454–2456.
46. Croitoru, M.; Bertsche, G.; Kern, D. P.; Burkhardt, C.; Bauerdick, S.; Sahakalkan, S.; Roth, S. Visualization and *In Situ* Contacting of Carbon Nanotubes in a Scanning Electron Microscope. *J. Vac. Sci. Technol., B* **2005,** *23*, 2789–2792.
47. Eklund, P. C.; Holden, J. M.; Jishi, R. A. Vibrational Modes of Carbon Nanotubes: Spectroscopy and Theory. In *Carbon Nanotubes*; Endo, M., Iijima, S., Dresselhaus, M. S., Eds.; Elsevier Science Ltd.: Oxford, UK, 1996; pp 129−142.
48. Moskovits, M. Surface-Enhanced Raman Spectroscopy: A Brief Retrospective. *J. Raman Spectrosc.* **2005,** *36*, 485–496.
49. Behr, N.; Raschke, M. B. Optical Antenna Properties of Scanning Probe Tips: Plasmonic Light Scattering, Tip-Sample Coupling, and Near-Field Enhancement. *J. Phys. Chem. C* **2008,** *112*, 3766–3773.
50. Zeeb, B. Fabrication of nanocone probe tips for optical near-field microscopy and vertical antenna arrangements. Diplom thesis, Eberhard Karls Universität Tübingen, 2010.
51. Yu, Z. H.; Brus, L. E. Reversible Oxidation Effect in Raman Scattering from Metallic Single-Wall Carbon Nanotubes. *J. Phys. Chem. A* **2000,** *104*, 10995–10999.
52. Teredesai, P. V.; Sood, A. K.; Govindaraj, A.; Rao, C. N. R. Surface Enhanced Resonance Raman Scattering from Radial and Tangential Modes of Semiconducting Single Wall Carbon Nanotubes. *Appl. Surf. Sci.* **2001,** *182*, 196–201.
53. Puech, P.; Anwar, A. W.; Flahaut, E.; Dunstan, D. J.; Bassil, A.; Bacsa, W. Raman G and D Band in Strongly Photoexcited Carbon Nanotubes. *Phys. Rev. B* **2009,** *79*, 085418.
54. Pettinger, B.; Ren, B.; Picardi, G.; Schuster, R.; Ertl, G. Tip-Enhanced Raman Spectroscopy (TERS) of Malachite Green Isothiocyanate at Au(111): Bleaching Behavior under the Influence of High Electromagnetic Fields. *J. Raman Spectrosc.* **2005,** *36*, 541–550.
55. Fleischer, M.; Weber-Bargioni, A.; Cabrini, S.; Kern, D. P. Fabrication of Metallic Nanocones by Induced Deposition of Etch Masks and Ion Milling. *Microelectron. Eng.* **2011,** doi:10.1016/j.mee.2011.02.090.
56. Cubukcu, E.; Kort, E. A.; Crozier, K. B.; Capasso, F. Plasmonic Laser Antenna. *Appl. Phys. Lett.* **2006,** *89*, 093120.